Compact superferric FFAG accelerators for medium energy hadron applications

B. Qin[a,*], Y. Mori[a]

[a]*Research Reactor Institute, Kyoto University, Kumatori, Osaka 590-0494, Japan*

Abstract

Medium energy hadron beams are desirable in various applications such as accelerator driven subcritical systems (ADSR), high intensity neutron sources and carbon therapy. Compactness and easy operation characters are important for this energy region, especially in the case of medical use purposes. This paper introduces a novel superferric scheme with scaling fixed-field alternating gradient (FFAG) accelerators, which can provide 400MeV/u carbon ions for cancer therapy. By employing a maximum field of 5T with a high field index, 8.5m diameter with 85cm radius excursion is achieved in a single FFAG ring. The lattice configuration and design of superferric magnet sectors with high permeability materials were described in detail. This scheme can also be extended to other hadron applications.

Keywords:
Superferric, scaling FFAG, medium energy hadrons, high permeability material

1. Introduction

Medium energy hadron beams (kinetic energy above 1.0GeV proton or 375MeV/u carbon ion), have important applications in accelerator-driven systems for nuclear energy, proton drivers for intense neutrons and muons, and carbon therapy. Existing candidate machines are synchrotrons, superconducting cyclotrons, linacs and FFAG accelerators. Superconducting magnets are widely employed since a high magnetic field can be achieved with very low power consumption using superconducting coils, that reduces the accelerator size and power consumption.

Since the first proof-of-principle proton FFAG synchrotron was developed at KEK in 2000[1], FFAG accelerators have undergone ten years of intense development, including both scaling and non-scaling categories [2, 3]. The world first ADSR prototype experiment was performed using a 150MeV FFAG complex, at KURRI in 2009 [4], and other plan to boost the energy to around 1GeV has been initiated. Some other designs for high energy, high power proton drivers using FFAGs have also been proposed [5, 6]. The characteristics of strong focusing and zero chromaticity in scaling FFAGs make them attractive in various applications. Furthermore, a small magnet aperture size with high field index and fast acceleration with fixed field renders this type of accelerator competitive versus synchrotrons and cyclotrons in the area of medium energy hadron beam applications, especially for carbon cancer therapy.

In recent years, clinical studies have shown that carbon ions have a larger biological effect on tissue than protons and X-rays, as well as being more effective on hypoxic radio-resistant tumors. In the meantime, carbon therapy has been transformed from being research oriented to clinically oriented. Four carbon therapy centers have been established, three in Japan and one in German. In 2009, among 16 proposals for hadron therapy facilities, 7 planned to employ carbon ions with energy of 400MeV/u [7].

Fundamental requirements of accelerators for carbon therapy are: (1)easy and reliable operation; (2) compactness and small size; (3) precise control of beam parameters such as dose rate, beam energy and intensity [8]. The same penetration depth, e.g. 25cm in water, requires 200MeV protons or 375MeV/u carbon ions, with a ratio of magnetic rigidity about 2.85. Therefore compactness becomes more important for carbon machines. Present medical centers for carbon therapy all employs synchrotrons with diameters larger than 20m. Some designs for hadron therapy accelerators using FFAGs have been proposed [9–13], with two representative projects: RACCAM [12], using a spiral sector scaling FFAG for proton therapy, and PAMELA [13] aiming at design and engineering of a non-scaling FFAG scheme for hadron therapy.

The main problem for applying scaling FFAGs to carbon therapy is controlling the radius excursion. High magnetic fields using a superconducting technique is a solution, and a $\cos\theta$ combined-function superconducting scheme has been applied to radial type FFAG magnets [14]. Compared with the ring consisting of radial triplet sectors (DFD or FDF), spiral ring is more compact due to a much lower circumference factor and hence are the ideal type for carbon therapy applications. However, it is difficult to apply combined-function superconducting coils to this type of sector.

To solve this problem, a superferric superconducting scheme for the spiral FFAG magnet is proposed. The layout contains one spiral FFAG ring, with momentum factor 4.9, corresponding to C^{6+} beam injection and extraction energy of 20MeV/u and 400MeV/u respectively, connected to a superconducting

*Corresponding author, Tel. : +81724512452.
Email address: bin-qin@rri.kyoto-u.ac.jp (B. Qin)

cyclotron or linac as the injector. A special hybrid-material magnet which combines low-carbon iron with high permeability material is adopted to achieve a maximum magnetic field of 5T with a moderate field index. The diameter of the FFAG ring can be limited around 8.5m, with 85cm orbit excursion. This paper is based on [15], with expansion and detailed considerations of lattice and magnet design.

2. Lattice design of the FFAG ring for carbon therapy

2.1. General consideration

The proposed overall accelerator layout is composed of one main spiral FFAG ring and an injector which delivers 20MeV/u C^{6+} beam. A superconducting cyclotron or IH linac could be the candidate injector. The schematic view is shown in Fig. 1.

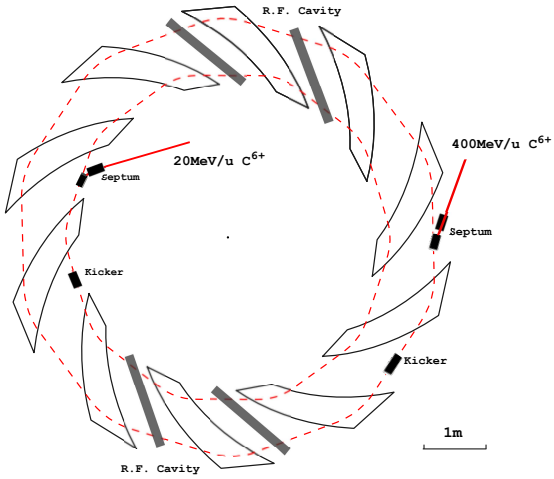

Figure 1: Schematic plan of the spiral FFAG ring for carbon therapy

The primary challenge is the high momentum ratio 4.9 for the single spiral FFAG ring which accelerates the carbon beam from 20MeV/u to 400MeV/u. From the scaling field law $B = B_0 \cdot (r/r_0)^k$ and $p = e \cdot B\rho = e \cdot B \cdot r \cdot pf$, the radius excursion can be expressed by:

$$\Delta r = ((p_{ext}/p_{inj})^{\frac{1}{1+k}} - 1) \cdot r_0 \quad (1)$$

where B_0 is the magnetic field corresponding to the reference radius r_0, and k is the field index. The packing factor pf is defined by $pf = \theta_m/\theta_{cell} = \theta_m/(2\pi/N)$, where θ_m is the open angle (angular width regarding to the ring center) of the spiral sector magnet, and N is the number of cells. A reasonable excursion should be less than 1m, since at present this value is the maximum aperture size of the rf cavity using metallic alloy (see section 2.3). To achieve this, a high field index and small r_0 (which means higher magnetic field as well) are necessary.

A linear matrix method was used for lattice parameters searching. The criteria are: (1) the field index k should be high enough to keep the magnet compact. (2) Spiral angle should be less than 60 degrees to provide enough drift space for installation of rf cavity . (3) The operational betatron tunes should be far away from low-order normal structural resonances. (4) The cell number N should be minimized to increase the drift space length at the same packing factor level. Cell number from 8 to 16 were scanned and $N = 10$ was determined to be optimum. Fig. 2 shows the corresponding working diagram in parameter space (k, ζ), where ζ is the spiral angle.

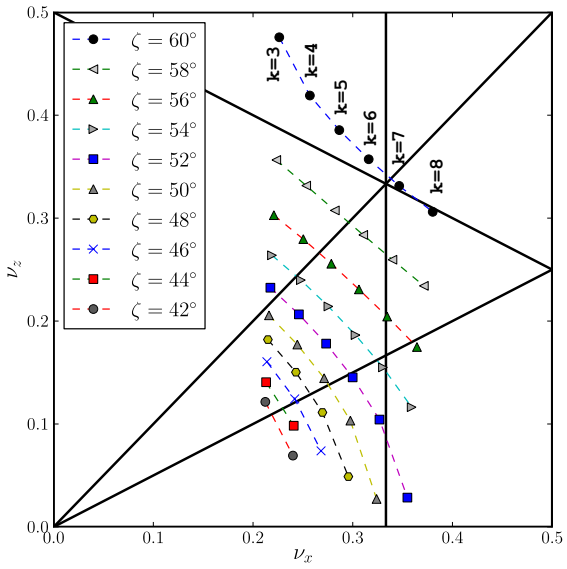

Figure 2: Cell tunes plot by lattice parameter searching with cell number $N = 10$, k range 3.0-8.0, ζ up to 60°. Normal structure resonances up to 3rd order are plotted

2.2. Lattice details

For a detailed lattice study including a transverse acceptance survey, four operating points aroud $k = 5$ in the tune diagram with reasonable ζ were chosen. The Zgoubi code with a FFAG-SPI procedure [16] was employed for full energy range simulation. For this case, the field distribution is expressed by:

$$B_z(r, \theta) = B_0 \cdot (r/r_0)^k \cdot \mathcal{F}(r, \theta - \ln r/r_0) \quad (2)$$

where $\mathcal{F}(r, \theta - \ln r/r_0)$ is the spiral azimuthal dependence of the field simulated by the Enge function $\mathcal{F}(d) = 1/(1 + exp(c_0 + c_1(d/g(r)) + ... + c_5(d/g(r))^5))$. d is the relative distance to the effective field boundary determined by r and θ, $g(r)$ is the gap size determined by:

$$g(r) = g_0 \cdot (r_0/r)^\kappa \quad (3)$$

and $c_0 \sim c_5$ are Enge coefficients.

With the fringe field distribution from Enge function, ray-tracing result can show the tune shift during acceleration. Estimation of acceptance is a purpose as well. Since the acceptance

is mainly decided by the working point, only c_0 and c_1 are set for simplification. They can approximately determine the fringe extent, which is the main source to affect the vertical tune.

The footprints at full energy of four chosen operating points are shown in Fig. 3, with corresponding lattice parameters listed in Table 1. In this full energy tracking, $\kappa = 0.6$ is assumed, the coefficients $c_0 = -0.005, c_1 = 0.95, c_{2\sim5} = 0$ are obtained from fitting of azimuthal field distribution calculated by TOSCA[17].

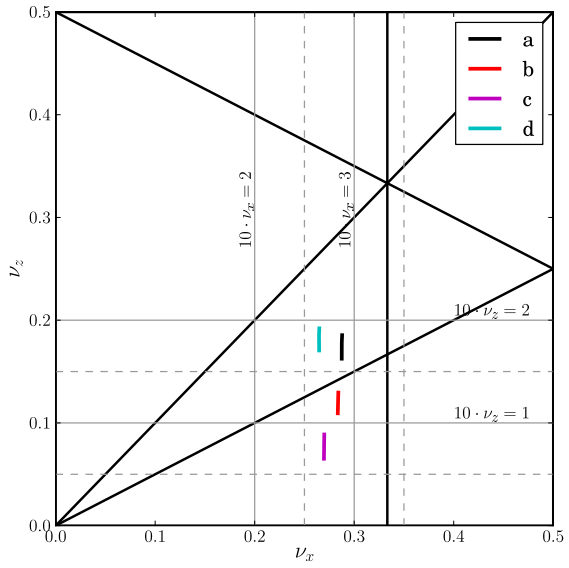

Figure 3: Footprint of 4 selected operating points at full energy range(20MeV/u to 400MeV/u), using the Zgoubi FFAG-SPI procedure, cell number $N = 10$. Solid lines are normal structural resonances up to 3rd order. Integer and half integer resonances of the ring tune are plotted as gray lines.

Transverse acceptances of four operating points are compared in Table 1. Results shows that vertical acceptances are comparable close. But the horizontal acceptance is affected by the position relative to the sextupole resonance and the horizontal phase advance. Lattice d is selected due to its much higher horizontal acceptance, as well as the spiral angle is moderate. The detail lattice parameters are shown in Table 2.

2.3. RF parameters for rapid acceleration

Spot scanning irradiation using narrow pencil beams is essential for cancer therapy, which requires a high repetition rate of the beam (100Hz-200Hz).

The sweep frequency of the RF system can be determined by the time of flight τ during acceleration with $\frac{\tau}{\tau_0} = (\frac{p}{p_0})^{\frac{-k}{k+1}} \cdot \frac{E}{E_0}$, since $\tau = \frac{C}{\beta c} = \frac{E \cdot C}{p \cdot c^2}$ and $\frac{C}{C_0} = \frac{r}{r_0} = (\frac{p}{p_0})^{\frac{1}{k+1}}$ according to the scaling law, where C is the circumference, and τ_0, p_0 are the time of flight and the momentum corresponds to the injection energy E_0.

In case of 5ms acceleration period with 200Hz repetition rate, the energy gain per turn $eV \sin\phi_s = 10$keV and total turns is $N = 38000$ are obtained from integrals of time of flight $T = \int \tau_{E_n} \cdot dN$ which fulfills $T = 4.9ms$. For synchronous

Table 2: Lattice of the carbon FFAG ring

Parameter	Value
Particle species	$^{12}C^{6+}$
Injector	superconducting cyclotron, or IH linac
Lattice type	spiral sector, scaling FFAG
Cell number	10
Injection/extraction energy	20 MeV/u, 400MeV/u
Injection/extraction rigidith	1.3T · m, 6.36T · m
Momentum ratio	4.9
Field index	4.6
Spiral angle	53.0°
Packing factor	0.37
Average orbit radius	2.55-3.4 m
B_{max} @ extraction	5.06T
ν_x/ν_z (cell tunes)	0.26 / 0.18
$\beta_x \quad min/max$ [1]	0.56 / 1.95 m
$\beta_y \quad min/max$ [1]	1.2 / 2.9 m
$D \quad min/max$ [1]	0.33 / 0.56 m

[1] Twiss parameters corresponds to the injection momentum

Table 3: Basic rf parameters

Parameter	Value
Repetition rate	200Hz
RF frequency	3.78MHz - 10.0MHz
Number of cavities	4
Harmonic number	1
RF peak voltage	5kV
γ_t	2.37
Field gradient	25kV/m
Radial aperture	90cm
Q	1.1

phase $\phi_s = 30°$ and 4 cavities installed, the peak voltage is about 5kV, corresponding to 25kV/m gradient for 20cm cavity length. The cyclic frequency varies from 3.78MHz to 10.0MHz during acceleration. The horizontal aperture of the cavity is 90cm, which is determined by radius excursion.

To achieve this high field gradient and very broad bandwidth, a high permeability magnetic alloy (MA) core [18] is required. This type of cavity has been proved to be efficient in the 150MeV FFAG ring developed at KEK [19], with a 35kV/m field gradient, low quality factor $Q \sim 1$ and large aperture of 1m. The basic RF parameters are listed in Table. 3, which are modest for an MA-loaded core technique.

3. Superferric magnet design

3.1. Superferric scheme using high permeability material

To fulfill magnet parameters in the proposed lattice, superconducting magnets has to be employed. Considering difficulties including design and fabrication for applying combined-function superconducting scheme to spiral sector magnets, we

Table 1: Parameters comparison of 4 selected working points (a-d)

Lattice	k	ζ	pf	Horizontal Acceptance (πmm · mrad)	Vertical Acceptance (πmm · mrad)
a	5.4	55.0	0.37	1300@inj. / 1800@extr.	240@inj. / 200@extr.
b	5.4	52.0	0.375	750@inj. / 360@extr.	260@inj. / 200@extr.
c	5.0	50.0	0.39	2900@inj. / 1400@extr.	370@inj. / 290@extr.
d	4.6	53.0	0.37	3500@inj. / 2400@extr.	450@inj. / 270@extr.

proposed the superferric scheme, which only employs superconducting coil to put high current on ferric magnet poles and simplifies coil design. This scheme has been applied to most superconducting cyclotrons. For reference, in cyclotrons, the field index $k \approx \gamma - 1$, is 0.5 even for 400MeV/u carbon ions and can be implemented by pole shaping. However, the field index for the proposed FFAG ring is much higher. Simulation results with the TOSCA code shows that by using iron poles, only $k < 2.0$ is feasible without trim coils, because the relative permeability μ_r of saturated iron at high field is almost equal to that of the air.

To achieve a high field index, some rare-earth metal such as holmium (Ho) or gadolinium(Gd), which have a higher permeability than air even in high field are preferred. The general feature of this type of material is its almost linear B-H curves with constant μ_r at different induction fields, below the Curie temperature. These materials have been applied in superferric quadrupoles and cyclotrons [20, 21], and measurement results show that at an induction magnetic field $B = 5T$, for Gd $\mu_r \approx 18.0$ and for Ho $\mu_r \approx 7.0$.

The proposed superferric magnet employs this type of high permeability material as the pole layer, but still uses iron as the return yoke, because a much higher μ_r in a non-saturated field reduces the yoke size. The illustration of this scheme is shown in Fig. 4. The cross section of the magnet can be separated into 3 layers: (1) the pole layer with high permeability Gd; (2) the non-saturated iron yoke; (3) the saturated iron area between (1) and (2).

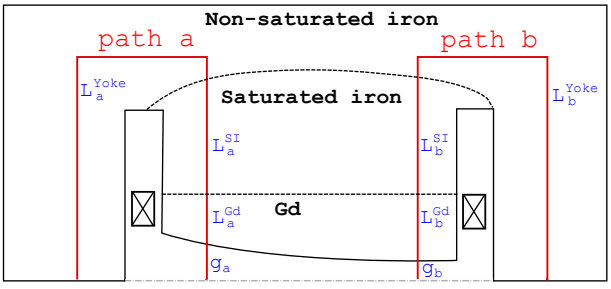

Figure 4: Superferric magnet scheme which combines iron yoke and high permeability pole material

Even using a high permeability layer, a constant field index can not be achieved by relying on the pole gap shape, and a designated layer geometry is required. A simulation study showed that for a simple layer configuration illustrated in Fig. 4 with the gap size defined by Eq. 3 ($\kappa = k$), the local field index k was far from the design value and the field at the extraction radius was much lower than the expected value. The reason was owing to the complex flux condition in multi-layer material configuration including saturated iron. For analysis, magnetic circuits were used. As shown in Fig. 4, two integral paths a and b were chosen at the injection and extraction radii. To establish the baseline situation of multi-layer material, magnetic circuits in a normal conducting ferric magnet can be expressed by Ampere's law:

$$\begin{aligned} NI &= \oint_{path-a} H \cdot dl \approx \frac{B_a \cdot g_a}{\mu_0} + \frac{B_a^{yoke}}{\mu_r^{iron}\mu_0} \cdot L_a^{yoke} \\ &= \oint_{path-b} H \cdot dl \approx \frac{B_b \cdot g_b}{\mu_0} + \frac{B_b^{yoke}}{\mu_r^{iron}\mu_0} \cdot L_b^{yoke} \end{aligned} \tag{4}$$

where B_a, B_b are mid-plane magnetic fields at integral paths a and b, g_a and g_b are corresponding gap sizes. Since for non-saturated iron, $\mu_r^{iron} \gg 1$, which eliminates the second term, the gap geometry forms a field gradient in Eq. 5:

$$g_a/g_b = (r_b/r_a)^k \implies B_b/B_a = (r_b/r_a)^k \tag{5}$$

In the superferric scheme with multi-layer materials, the magnetic circuit at path a is given by:

$$\begin{aligned} \oint_{path-a} H \cdot dl \approx \frac{B_a \cdot g_a}{\mu_0} + \frac{B_a^{Gd} \cdot L_a^{Gd}}{\mu_r^{Gd} \cdot \mu_0} + \frac{B_a^{SI} \cdot L_a^{SI}}{\mu_r^{SI} \cdot \mu_0} \\ + H_{yoke} \cdot L_{yoke} \end{aligned} \tag{6}$$

where the superscripts Gd and SI correspond to gadolinium and saturated-iron layers. A similar equation applies to path b. Only the term $H_{yoke} \cdot L_{yoke}$ can be neglected. To fulfill Eq. 5, the sum of reluctance in Gd and saturated-iron should be balanced for different integral paths. Since $\mu_r^{Gd} \sim 20$ and $\mu_r^{SI} \sim 2$, $B^{SI}L^{SI}/\mu_r^{SI}\mu_0$ is the dominant term. $L_b^{SI} < L_a^{SI}$ can be derived from $B_b^{SI} > B_a^{SI}$. With a reasonable assumption, $L_a^{Gd} + L_a^{SI} \approx L_b^{Gd} + L_b^{SI}$, we have the general requirement that $L_b^{Gd} > L_a^{Gd}$, and the thickness of the Gd layer should be modulated along the radius. However, an analytical relation can not be established due to the nonlinearity of magnetic materials. We used a geometry length function given by:

$$L^{Gd}(r) = d_0 + d_1/g(r)^m \tag{7}$$

where d_0, d_1 and m are empirical coefficients by parameters search using TOSCA.

3.2. Procedures of magnet modeling and optimization

For spiral sector scaling FFAG magnet using variable pole gap, the purpose of magnet modeling and optimization is to control the chromaticity during beam acceleration, especially for the vertical tune which will be enlarged due to the decreased fringe extent caused by the smaller gap size at higher beam energy. Experience from the design of the RACCAM prototype magnet [22] has demonstrated the compensation of the tune shift by optimizations on the pole shape.

This section describes a series of procedures for sophisticated 3D magnet modeling and optimization. To clarify them in logical view, a flow chart is shown in Fig. 5.

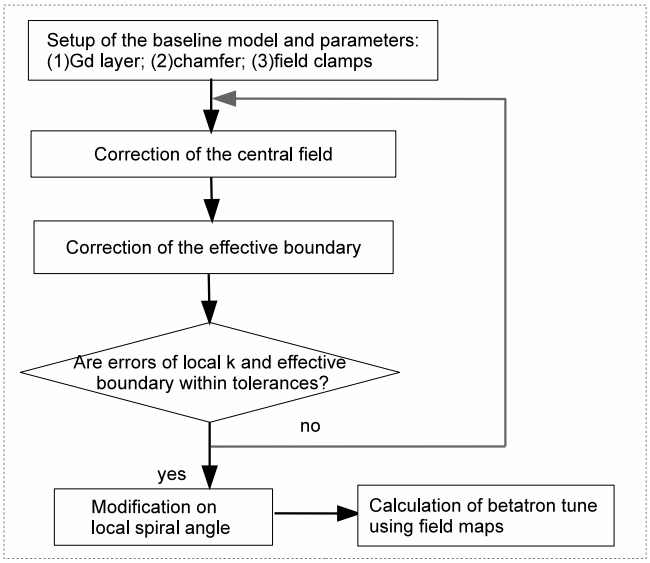

Figure 5: Flow chart for procedures of magnet modelling and optimization

The first step is to setup the baseline of the magnet geometry, including the configuration of Gd layer, the pole chamfer and field clamps. Study shows the field index has a sensitive dependency on the thickness of Gd layer. For parameters search of Eq. 7, linear element model with TOSCA was used for conservation of computation time. The criteria lies on that errors of the central magnetic field are within ±10% compare to the theoretical value obeying the scaling law. For the proposed magnet parameters, $d_0 = 12.0$, $d_1 = 65.0$, $m = 2.1$ are determined.

By introducing a pole chamfer and field clamps, the fringe field extent and the change in field flutter along the radius can be reduced, Study shows that a variable width pole chamfer with increased size along the radius will compensate the natural field flutter growth due to a smaller pole gap. Field clamps are very effective to narrow the fringe field extent, as well as to decrease the change in flutter. In a high field situation, the thickness and material are important factors.

After the setup of a baseline model, a sequence of iterative optimizations need be performed, for the purpose of limiting transverse betatron tune shifts to avoid dangerous resonance crossing. The following three routines are applied:

1. Correction of the central magnetic field (at the middle line of the spiral sector) by gap shaping of the magnet pole. The initial pole gap is constructed using Eq. 3 with $\kappa = k$. Then the calculated central field $B_{cen}^{model}(r)$ is compared with the theoretical value $B^{theo}(r)$ given by the scaling law, and the new gap size $g'(r)$ is calculated from previous value $g(r)$ by:
$$g'(r) = g(r) \cdot B_{cen}^{model}(r)/B^{theo}(r) \tag{8}$$
2. Correction of the effective magnetic field boundary based on calculation of the field integrals $\int B_z \cdot dl$. This method has proved to be efficient for alignment of the local spiral angle and local field index determined by field integrals, thus stabilizing transverse focusing. By using the method introduced in [22], the effective field boundary $L_{entrance\,|\,exit}^{eff}$ can be calculated by field integrals along the *entrance* and *exit* path of reference orbits at each side of the center of the magnet sector (Eq. 9). Then these radius dependent results are compared to the fixed theoretical field boundary $L^{theory} = (\pi/N) \cdot R \cdot pf$, and iterative pole geometry modifications are performed to reduce this difference. Meantime, the local spiral angle, which is directly determined by the effective field boundary, is aligned to the design value.
$$L_{entrance\,|\,exit}^{eff} = (\int B_z \cdot dl)_{entrance\,|\,exit}/B_z^{center} \tag{9}$$
3. Modification of the local spiral angle, to compensate for the vertical tune shift after optimization using the former methods. In the case of cell number $N \gg 1$, transverse tunes can be estimated using first order approximation:
$$\nu_x^2 \approx 1 + k \tag{10}$$
$$\nu_z^2 \approx -k + F \cdot (1 + 2\tan^2\zeta) \tag{11}$$
Stable ν_x can be obtained by a local field index correction, but for ν_z, even after a good alignment with local ζ, the field flutter remains about 20% difference between injection and extration radii. Since k should be constant, the only free knob is the local spiral angle ζ. By using the derived Eq. 12 and observed $\delta\nu_z$, the minute change of local spiral angle $\delta\zeta$ can be estimated from local ζ and average F.
$$\frac{d\nu_z}{d\zeta} = \frac{2F \cdot \tan\zeta}{\sqrt{-k + F(1 + 2\tan^2\zeta)} \cdot \cos^2\zeta} \tag{12}$$

As shown in Fig. 5, the first two routines are combined in one iteration. Normally after 5 iterations, errors of the local field index and the effective boundary can be controlled within the tolerance (suggested tolerance ±2% for the local field index, and ±0.5% for the effective boundary), then the third routine on local spiral modification is proceeded. The betatron tunes calculated from particle tracking on the extracted field map is the final reference for the magnet optimization.

3.3. Prototype magnet modeling and beam dynamics results

A prototype superferric magnet has been modeled using TOSCA Preprocessor, which is demonstrated in Fig. 6. The magnet parameters are listed in Table 4. Compared with the lattice parameters (see Table 2), only the packing factor increased

Table 4: Parameters of the magnet model

Parameter	Value
Field index	4.6
Spiral angle	53 degree
Packing factor	0.38
Open angle	13.68 degree
Radial expand of the magnet pole	2.4m-3.6m
Total weight (one sector)	21 tons
Total current of the coil	182kA · T

to 0.38. A variable length Gd pole layer is combined with an iron yoke. Field clamps with a constant gap size using the same Gd material are used to limit the field extent. The thickness of the clamp influences field flutter and is modulated along the radius. At the injection radii where significant decrease of the field flutter exists, the clamp has a maximum thickness of 5cm.

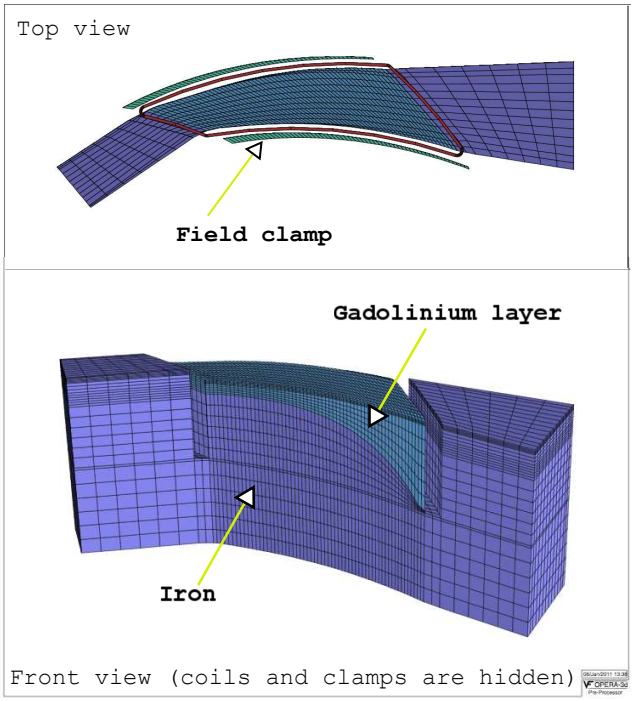

Figure 6: TOSCA model of multi-layer superferric spiral sector

Iterative procedures on the sector pole geometry described in section 3.2 are performed. To demonstrate the comparative results, three models are picked up. model2 is the initial model, model7 is the model after correction of the central field and the effective boundary with 5 iterations, and the final model7-v4 is the model after modification on the local spiral angle. The corrections are performed in good field region (2.5-3.4m) on radial dimension, which covers the pole radius from injection 2.51m to extraction 3.37m. As shown in Fig. 7 and Fig. 8, by comparing model7 with model2, errors of effective field boundary are controlled within ±0.5%, and both local field index and central magnetic fields are well aligned to the design value.

Transverse tunes covering the full energy region are calcu-

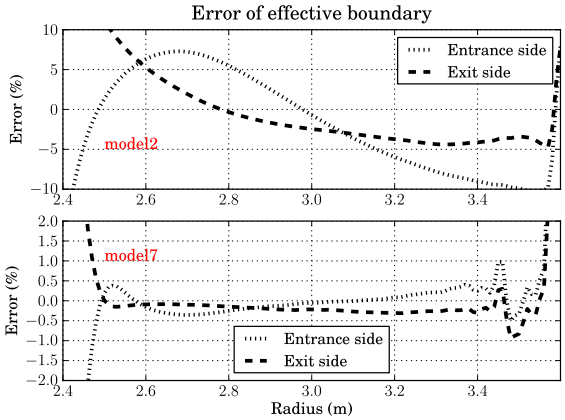

Figure 7: Effective boundary error of the magnet models, with the error calculated by $\delta = (L^{eff}_{entrance|exit} - L^{theory})/L^{theory}$. (top) model2; (bottom) model7.

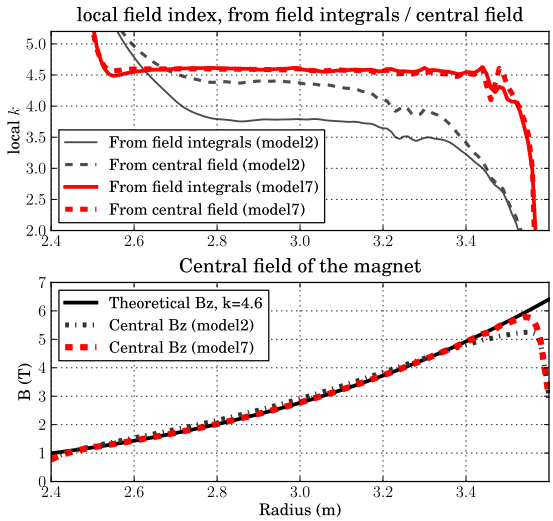

Figure 8: (top) local field index calculated from field integrals and central field of the magnet sector; (bottom) central field distribution along the radius, comparison to theoretical value from scaling law

lated by the Zgoubi code on 2D mid-plane TOSCA field maps, and evolution during the model optimization procedure is shown in Fig. 9. It can be observed for model7 after effective boundary correction, ν_x is stable around 2.6 and the vertical tune shift is abbreviated to $\Delta\nu_z < 1.0$, compared to model2. For model7-v4 which has a more stable ν_z, a linear modification of the local spiral angle was adopt according to Eq. 12, with $\delta\zeta = 0.07°/cm$ from $R = 300cm$ to $R = 244cm$, and $\delta\zeta = -0.02°/cm$ from $R = 302cm$ to $R = 340cm$.

Horizontal and vertical beam acceptances are also estimated, shown in Fig. 10 and Fig. 11. For horizontal acceptances, the average value is about 3000πmm · mrad.; for the vertical situation, 390πmm · mrad and 180πmm · mrad corresponding to the injection and extraction energy respectively. These acceptances have a good match to the estimation from the Enge model in Section 2.2.

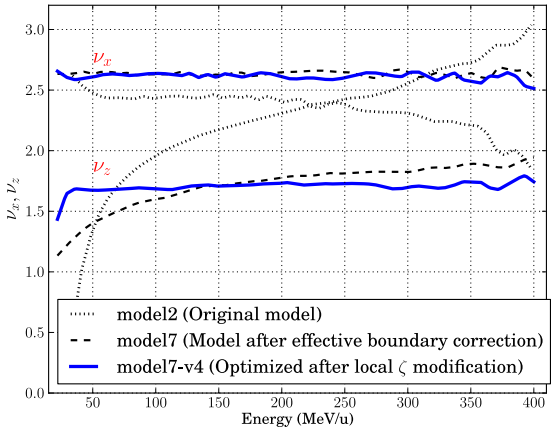

Figure 9: Evolution of the transverse tunes of the ring during model optimization procedure, calculated by Zgoubi using 2D TOSCA maps.

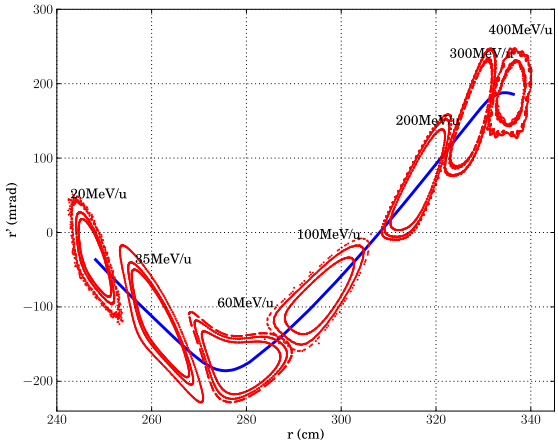

Figure 10: Horizontal stability region of beam phase space, along the radius. Initial vertical deviation $z_0 = 1mm$ is assumed. The acceptance is estimated by $\epsilon = x_{max}^2/\beta$, where β is calculated from small amplitude phase space, and x_{max} is the radial deviation to the center of the phase space corresponding to the maximum stable phase space envelope.

4. Conclusion and discussion

This paper shows the feasibility of using a compact superferric scaling FFAG with spiral sectors for carbon therapy applications. Detailed methods and procedures relating to the design of lattice and superferric magnet are described. The design can also be transferred to other applications that use medium energy hadron beams. The merit of this scheme is that a small size ring with an 85cm radius excursion can be achieved when accelerating carbon ions up to 400MeV/u with a single spiral FFAG ring. It is also possible to use a fast spot scanning mode in cancer therapy with high repetition rate and rapid acceleration.

At present, there exist some issues which are beyond the scope of this paper.

1. The detailed experimental results of high permeability materials, such as the B-H curve dependence on temperature; For Gd which has a high Curie point of about 290K, optional working points exist below this temperature. Higher permeability is possible and desired, which renders better field quality and eases the magnet design and construction.
2. Practical issues related to carbon therapy, such as control of dose rate and conformity, beam transfer and gantry design, variable energy scheme etc. These factors are important for clinically oriented demands and require detailed study.

Acknowledgement

This study was supported by Japan Science and Technology Agency under Strategic Promotion of Innovative Research and Development Program.

We would like to thank F. Meot, BNL, for his valuable helps on the code Zgoubi. We also express our thanks to T. Planche, K. Okabe and T. Uesugi, Kyoto University, for their fruitful discussions and comments.

References

[1] M. Aiba et al., Development of a FFAG proton synchrotron, Proc. of EPAC00, 2000, pp. 581-583 (2000).
[2] Y. Mori, FFAG Accelerators and Their Applications, Proc. of EPAC'06, Edinburgh, 2006, pp.950-954.
[3] Y. Mori, Development of FFAG accelerators and their applications for intense secondary particle production, Nucl. Instr. Meth. A, 563(2006) 591-595.
[4] Y. Ishi, et al., Present status and future of FFAGs at KURRI and the first ADSR experiment, Proc. of IPAC10, Kyoto, 2010. p. 1323.
[5] Y. Mori, FFAG proton driver for muon source, Nucl. Instr. Meth. A, 451 (2000) 300-303.
[6] Alessandro G. Ruggiero. FFAG based Proton and Heavy Ion High Power Drivers, ICFA Beam Dynamics Newsletter No. 43, 2007.
[7] U. Amaldi et al., Accelerators for hadron therapy: From Lawrence cyclotrons to linacs, Nucl. Instr. Meth. A, 620(2010) 563-577.
[8] S. Peggs, T. Satogata, J. Flanz, A survey of hadron therapy acceleration technologies, Proc. of PAC 07. 115-119.
[9] T. Misu et al., Design study of compact medical fixed-field alternating-gradient accelerators, PRST-AB, vol. 7, 094701 (2004)
[10] E. Keil, A. M. Sessler, D. Trbojevic, Hadron cancer therapy complex using nonscaling fixed field alternating gradient accelerator and gantry design. Phy. Rev. STAB, 10, 054701 (2007).
[11] C. Johnstone, S. Koscielniak, New nonscaling FFAG for medical applications, Proc. of PAC 07, 2951-2953.
[12] S. Antoine et al., Principle design of a protontherapy, rapid-cycling, variable energy spiral FFAG, Nucl. Instr. Meth. A, 602 (2009) 293-
[13] T. Yokoi, Overview of PAMELA project : an approach to particle therapy using NS-FFAG, IEEE Nuclear Science Symposium Conference Record, 4158-4162.
[14] T. Obana et al., Prototype superconducting magnet for the FFAG accelerator, Fusion Engineering and Design 81 (2006) 2541-2547.
[15] B. Qin, Y. Mori, A superferric superconducting scheme using spiral FFAG for carbon therapy. FFAG Int. Workshop 2010, KURRI, Osaka, Oct. 28-31.
[16] J. Fourrier et al., Spiral FFAG lattice design tools. Application to 6-D tracking in a proton-therapy class lattice, Nucl. Instr. Meth. A, 589 (2008) 133-142.
[17] Opera-3D User Guide,Vector Fields Limited, England.
[18] C. Ohmori, et al, MA-loaded cavity for barrier bucket experiments, EPAC98, 1796-1798.

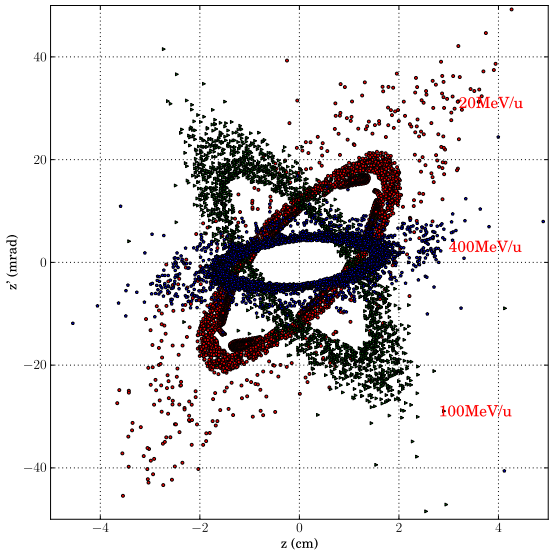

Figure 11: Vertical stability region of beam phase space, at three energy spots. The acceptance is estimated using same method as the horizontal case.

[19] Y. Yonemura, et al., Development of RF acceleration system for 150 MeV FFAG accelerator, Nucl. Instr. and Meth. A 576 (2007) 294-300.

[20] D.B. Barlow et al., Compact high-field superconducting quadrupole magnet with holmium poles. Nucl. Instr. Meth. A, 313(1992) 311-314

[21] J. Zhang et al., Preliminary study on a compact high field superconducting isochronous cyclotron K250-42 megatron. CYCLOTRON 2010, Lanzhou, China, 2010 Sept. 6-10.

[22] T. Planche et al., Design of a prototype gap shaping spiral dipole for a variable energy proton therapy FFAG, et al., Nucl. Instr. Meth. A, 604 (2009) 435-442.